NUCL SCI TECH (2019) 30:94
https://doi.org/10.1007/s41365-019-0625-z

Calculation of the heat flux in the lower divertor target plate using an infrared camera diagnostic system on the experimental advanced superconducting tokamak

Zhi-Xue Cui[1] · Xin Li[2] · Shuang-Bao Shu[2] · Jia-Rong Luo[1] · Mei-Wen Chen[3] · Yu-Zhong Zhang[2]

Received: 11 August 2018 / Revised: 25 February 2019 / Accepted: 1 March 2019 / Published online: 15 May 2019

Abstract During the discharging of Tokamak devices, interactions between the core plasma and plasma-facing components (PFCs) may cause exorbitant heat deposition in the latter. This poses a grave threat to the lifetimes of PFCs materials. An infrared (IR) diagnostic system consisting of an IR camera and an endoscope was installed on an Experimental Advanced Superconducting Tokamak (EAST) to monitor the surface temperature of the lower divertor target plate (LDTP) and to calculate the corresponding heat flux based on its surface temperature and physical structure, via the finite element method. First, the temperature obtained by the IR camera was calibrated against the temperature measured by the built-in thermocouple of EAST under baking conditions to determine the true temperature of the LDTP. Next, based on the finite element method, a target plate model was built and a discretization of the modeling domain was carried out. Then, a heat conduction equation and boundary conditions were determined. Finally, the heat flux was calculated. The new numerical tool provided results similar to those for DFLUX; this is important for future work on related physical processes and heat flux control.

Keywords EAST · Divertor target plate · Infrared camera · Heat flux · Finite element analysis

1 Introduction

In Tokamaks, the plasma energy generated by either ohmic heating, auxiliary heating, or fusion reaction is eventually deposited into the plasma-facing components (PFCs). As the auxiliary heating power increases and the discharge times are prolonged, the temperature of PFCs may become extremely high, which poses a grave threat to the lifetime of the PFCs materials [1–3]. To operate under extreme conditions and long plasma pulses, PFCs materials must not only withstand high heat flux but also demonstrate particle exclusion ability. Research on the heat flux of PFCs can improve the safe and steady operation of the device and helps determine methods to actively control heat flux.

Most heat flux calculation methods require the temperature data of PFCs as inputs to determine the evolution of heat flux over time. However, contact thermocouples cannot be used to acquire heat flux because of their long response time and low spatial resolution. In the case of the EAST thermocouple system, there are only ten thermocouples in one port, so measurements are limited by the number of contacts with the thermocouples. As for the time resolution of the thermocouples, the response time is nearly 0.5 s, which is much longer than the acquisition time of an infrared camera. Spectrometers are good tools to measure temperature; however, they only measure the temperature

This work was supported by the National Natural Science Foundation of China (Nos. 51505120 and 11105028), and the National Magnetic Confinement Fusion Science Program of China (No. 2015GB102004).

✉ Shuang-Bao Shu
shu@hfut.edu.cn

1 College of Information Sciences and Technology, Donghua University, Shanghai 201620, China

2 School of Instrument Science and Opto-electronics Engineering, Hefei University of Technology, Hefei 230009, China

3 Institute of Plasma Physics, Chinese Academy of Sciences, Hefei 230031, China

of a small area, so they are not ideal for calculating the heat flux distribution. For these reasons, infrared (IR) cameras, which have been installed in the diagnosis systems of different Tokamak devices, including those of Tore–Supra, JET, ASDEX Upgrade, and NSTX, are considered excellent tools to obtain the temperature distribution at large spatial resolutions [4–7]. At present, the finite difference program, DFLUX, is used to calculate the heat flux on the lower divertor plate of EAST [8], which needs the temperature data of PFCs as an input. In this paper, we propose the finite element method as an alternative method to determine heat flux, compared with DFLUX as a consistency check.

The rest of the paper is organized as follows: Section 2 presents the infrared diagnostic system used in this study. Section 3 describes the calculation method, using the finite element method, to determine the heat flux occurring on the divertor plate. Section 4 presents the experimental results and analysis, and Sect. 5 provides conclusions.

2 Infrared diagnosis system

EAST is the first fully superconducting Tokamak with a noncircular cross section in the world; it was developed by the Institute of Plasma Physics of the Chinese Academy of Sciences and aims to conduct steady-state and long-pulsed plasma discharges [9–11]. Because the observation ports of EAST are scarce, the monitoring system cannot occupy arbitrary ports. The locations of the components installed in the EAST device are arranged to meet the demands of several diagnostic systems. Hence, according to the structural characteristics and the location of its diagnostic port on EAST, a set of mid-waveband IR/visible integrated endoscope monitoring systems was developed. Here, the IR and visible thermal cameras share a single optical path. As shown in Fig. 1, 16 observation ports were installed in EAST for the related diagnostic systems, and the IR diagnostic system applied to this work, which consists of an IR camera and an endoscope system, is installed in port K. The IR diagnostic system has a large field of view (47° × 58°) and can simultaneously monitor images in port N, O, and P.

As shown in Fig. 2, the endoscope system is composed of an endoscope head, including a head parabolic mirror and a head plane mirror with a small aperture, a collimating lens, a sealed port, and a spectroscope; the endoscope system itself is based on the principle of pinhole imaging.

To realize full use of the aperture of the IR band system, the separation of the visible and IR light paths is achieved by inserting a splitter in the optical path. The spectroscope is used to penetrate the IR band and then to reflect the visible band. The diagnostic system is composed of the endoscope system (Fig. 2), a visible light-receiving system, and an IR light-receiving system. The front end of the endoscope determines its field of view, and its caliber is 180 mm. The system adopts the off-axis design method, which expands the field of view and darkens unimportant imaging areas. Because of the large heat load produced by EAST during discharge, a glass material with a coefficient of thermal variation in approximately zero is used as the mirror substrate to prevent the reflective material from deforming. The detector can be separated from the optical system to improve its ease of use. Two fine-tuning platforms with the detector were installed, and the latter can be adjusted by loosening or tightening the screws under the platform. The endoscope deviates from the middle plane by 145 mm and rotates 5° clockwise relative to the window with the optical axis.

The IR camera used in this system is a FLIR SC700BB camera with a wave range of 2.5–5 µm. The maximum frame rate of this camera is 2000 frames per second (fps) for reduced resolution and 100 fps for full-frame resolution (640 × 512 px^2). The spatial resolution of the camera at the divertor target plate is 4 mm. As shown in Fig. 3, the IR camera can monitor the upper divertor, the lower

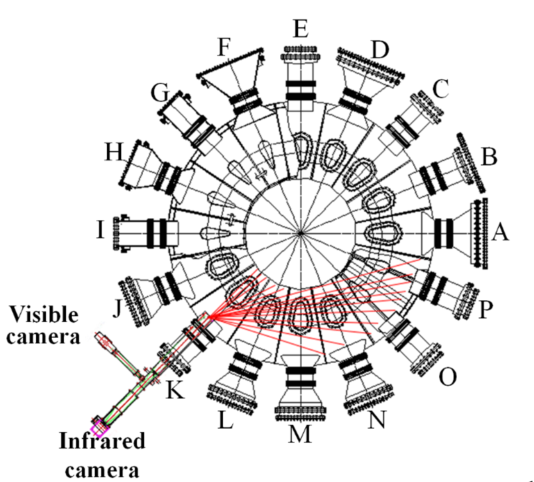

Fig. 1 Top view of the IR diagnostic system in EAST

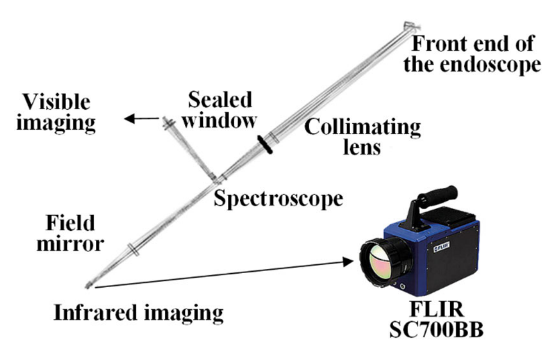

Fig. 2 Endoscope system

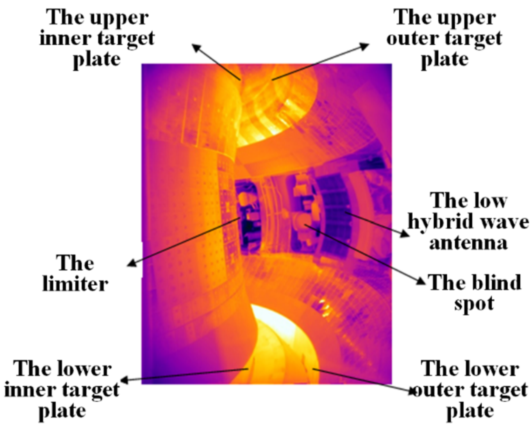

Fig. 3 (Color online) Image obtained by the IR diagnostic system

divertor, the low hybrid wave antenna at port N, and the limiter located between port M and port N simultaneously.

3 Heat flux calculation

The flowchart of the heat flux calculation program proposed in this paper is shown in Fig. 4. First, the true temperature of the LDTP in the radial direction is obtained by calibrating the surface temperature read by the IR camera. Next, a target plate model is built according to the physical structure of the LDTP and a discretization of the modeling domain is generated (100 cells in radial direction and 12 cells in depth direction). The initial condition of the modeling domain is set to 25 °C, and the boundary condition is the temperature data obtained from the IR camera. The heat conduction equation was solved according to the initial and boundary conditions, to determine the target plate model. Finally, we needed to adjust the parameter (R_s) that is introduced below to obtain a more accurate heat flux result.

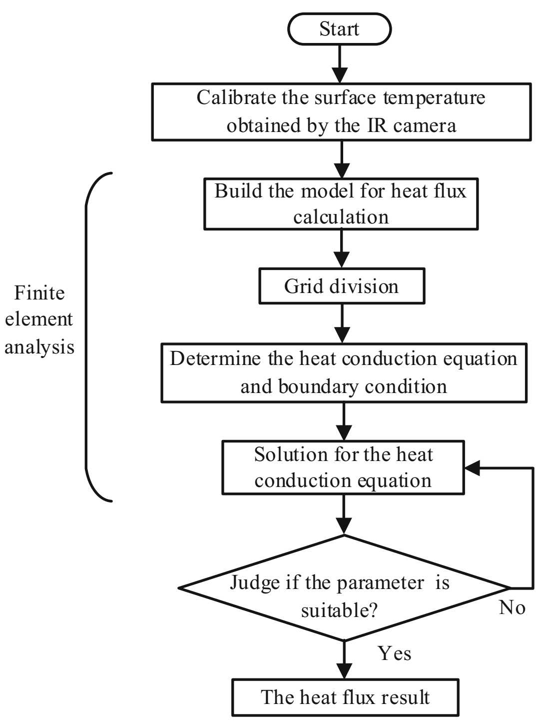

Fig. 4 Flowchart of the heat flux calculation using the finite element method

3.1 The calibration of surface temperature

Owing to the effects of material emissivity [12, 13], the IR transmissivity of the endoscope system, and the response function of the IR camera, the temperature obtained directly by the IR camera shows marked deviations from the true temperature; thus, it cannot be used to calculate the heat flux directly. The built-in thermocouple of EAST can obtain true temperatures under baking conditions because the temperature changes slowly, which provides the best opportunity to calibrate the temperature obtained by the IR camera. The calibration result is shown in Fig. 5; here, the x-axis indicates the LDTP temperature measured by the IR camera and the y-axis indicates the LDTP temperature measured by the built-in thermocouple of EAST. The fitting result shown in Fig. 5 reveals a good relationship between the temperature obtained by the IR camera and the true temperature, such as the root-mean-square error E_{RMSE} is 0.998 and the correlation coefficient R is close to 1, so these calibration results meet the requirements of the application.

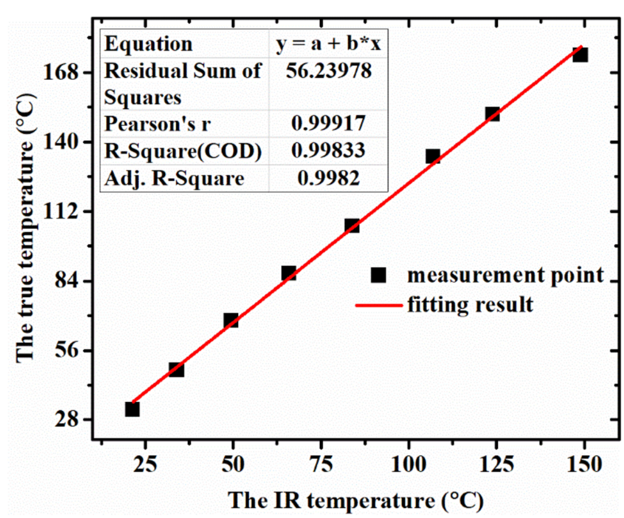

Fig. 5 Calibration of surface temperature on the LDTP

3.2 The structural model and grid division

The LDTP is made up of 20-mm-thick graphite, which can interact with the scrape-off plasma layer. This interaction forms a thin layer on the graphite surface, and the heat conduction property and thickness of this layer are unknown. The heat sink layer is a copper–chrome–zirconium (CuCrZr) alloy, 22-mm thick, which connects the graphite layer to a soft graphite layer. Based on the physical structure of the LDTP, the heat flux calculation model is built and illustrated in Fig. 6.

The model assumes that there is no heat conduction in the toroidal direction owing to the symmetry of the LDTP in the toroidal direction. Hence, the x-axis is the radial direction and the y-axis is the depth direction. Moreover, the thickness of the soft graphite layer is only 0.5 mm, and its thermal conductivity is high; thus, this layer is ignored in the heat flux calculation. However, the thin layer cannot be ignored because the thermal conductivity is extremely low and it exerts a strong thermal insulation effect. As the thickness of this layer is far less than the thickness of the soft graphite layer, a discretization of the thin layer is not needed. The heat flux calculation model includes two types of boundary conditions and one type of initial condition: The thin layer surface which is determined from the temperature data collected during discharge, the adiabatic layer which assumes no transitive heat, and the initial condition of the modeling domain is set to 25 °C. The discretization of the target plate model, generated according to the pixel resolution of the IR camera and the physical structure of LDTP, is shown in Fig. 6.

3.3 The heat flux calculation equation

According to Fourier's law of heat transfer, the heat flux (dQ) of an infinitely small area (dS) flowing through the normal direction over an infinitesimal period (dt) is proportional to the derivative of the temperature ($\partial T/\partial n$) along the normal direction (n) of the solid material surface. Thus, heat flux can be expressed as:

$$\mathrm{d}Q = -k(x,y,z)\frac{\partial T}{\partial n}\mathrm{d}S\mathrm{d}t, \tag{1}$$

where $k(x, y, z)$ is the heat conductivity of the material at the point (x, y, z), and the negative sign in Eq. (1) indicates that heat flows from a location of higher temperature to one of lower temperature. In the heat flux model of this study, the heat flux $q(x, y = 0, t)$ at position x of the graphite layer and time t can be expressed as:

$$q(x,y=0,t) = k\cdot\frac{T(x,y=0,t)-T(x,y=d_{\mathrm{y}},t)}{d_{\mathrm{y}}}, \tag{2}$$

where $T(x, y = 0, t)$ is the surface temperature at position x of the graphite layer surface and at time t and $T(x, y = d_y, t)$ is the temperature at time t of the point that is d_y away from the graphite layer surface in the normal direction. k is the heat conductivity of graphite, which is the same as that of the DFLUX source code. The total surface heat power during discharge can be expressed as:

$$\mathrm{power} = \int_0^{t_{\mathrm{up}}}\int_0^{x_{\mathrm{up}}} k\cdot\frac{T(x,y=0,t)-T(x,y=d_{\mathrm{y}},t)}{d_{\mathrm{y}}}\mathrm{d}x\mathrm{d}t, \tag{3}$$

where t_{up} is the maximum value of the discharge time and the most discharge data obtained by IR camera are 10 s. Here, x_{up} is the maximum value in the x-axis direction, which is 0.32 m in this model (80 px in the IR image). To obtain the surface heat flux, we also need to know the temperature at all grids at all times.

The temperatures at every time are calculated by the heat conduction equation and appropriate boundary conditions. The heat conduction equation in this model can be expressed as:

$$\rho c\frac{\partial T}{\partial t} = \frac{\partial}{\partial x}\left(k_{\mathrm{x}}\frac{\partial T}{\partial x}\right) + \frac{\partial}{\partial y}\left(k_{\mathrm{y}}\frac{\partial T}{\partial y}\right), \tag{4}$$

where ρ is the density of the material, c is the specific heat capacity of the material, and k_x and k_y represent the components of the heat conductivity on the two axes. As the present system includes two different materials, all parameters of these materials are selected for each layer, and the values of these parameters are obtained from the source code of DFLUX. The boundary conditions in this model consist of the adiabatic boundary condition and the temperature boundary condition. The equation of the adiabatic boundary condition can be expressed as:

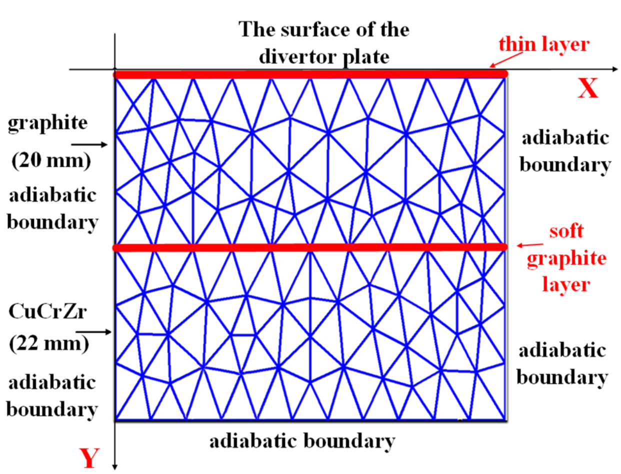

Fig. 6 Sketch map of the grid division of the divertor plate

$$\frac{\partial T}{\partial n} = 0. \tag{5}$$

Equation (5) indicates that heat is not transferred in the adiabatic layer. The equation of the temperature boundary condition can be expressed as:

$$T_{\mathrm{up}}(x,t) = T_{\mathrm{IR}}(x,t), \tag{6}$$

where $T_{\mathrm{IR}}(x, t)$ is the temperature at a certain position and time, which can be obtained by calibrating the surface temperature as determined by the IR camera on the LDTP, and $T_{\mathrm{up}}(x, t)$ is the temperature of the upper surface of the thin layer in the model at a certain position and time. Heat transmission in the thin layer can be considered 1D, i.e., only the y direction. The heat conduction equation of the thin layer can be expressed as follows:

$$\rho c \frac{\partial T}{\partial t} = \frac{\partial}{\partial y}\left(k \frac{\partial T}{\partial y}\right). \tag{7}$$

As the material of the thin layer is unknown, the k in Eq. 7 is also unknown. However, k is related to the thermal resistance (R_{s}) and thickness (d_{y}) of the thin layer, and this relationship can be expressed as:

$$k = d_{\mathrm{y}}/R_{\mathrm{s}}. \tag{8}$$

The d_y is set as 0.01 mm which is thin enough because it is far less than 4 mm, and Eq. 8 can be replaced in Eq. 7. To solve Eq. 7, we used the fixed value of *rho* and c; however, these values do not have any practical significance and do not interact with the physical parameters of the thin layer. They simply are two values for calculating the temperature of the lower surface of the thin layer. To get the real temperature value of the thin layer lower surface, we change the parameter R_{s} to get different temperature values until meeting the simple criterion first proposed in the NSTX Tokamak, i.e., an appropriate R_{s} should be selected such that the deposited energy is kept constant. Here, we select an R_{s} value that can keep the energy deposition constant after discharge since no more power arrives at the divertor [17, 18]. However, this method only produces an approximate result owing to the four factors that affect the heat flux result after the end discharge. They are surface heat dissipation after the end discharge, the accuracy of temperature measurement; the heat flux method which uses the assumption of circumferential symmetry, but are not strictly symmetrical, and the gradual process of plasma current drop.

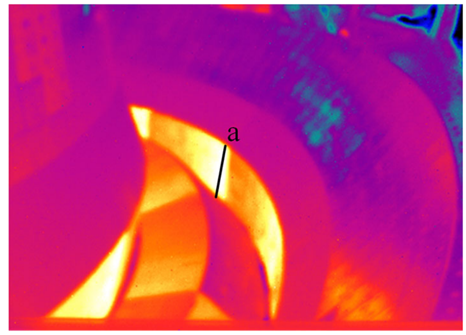

Fig. 7 (Color online) Selected line to calculate the heat flux for on LDTP

4 Experimental results and analysis

Figure 7 shows that the temperatures are different in the circumferential direction; the theory behind this is yet to be studied. We can only obtain the heat flux results for a line because of the assumption of circumferential symmetry in the current heat flux calculation program. We chose the line in Fig. 7 in this study. To calculate the heat flux result, different R_{s} were selected to calculate the heat flux of shot #56028 based on the above criteria, and the time evolution of energy deposition of the line at a different R_{s} is shown in Fig. 8. The top-left legend in Fig. 8 illustrates the six R_{s} values used in the calculation, and the red-dashed line in the figure indicates that the discharge is disrupted at approximately 8.4 s. Energy deposition decreased with an underestimated R_{s} after switch-off of the external heating but increased with an overestimated R_{s}. In this case, the optimum R_{s} for shot #56028 is 2×10^{-5} m ^{2} K/W.

Figure 9 exhibits the discharge condition of shot #56028 at the lower single null (LSN) magnetic field configuration, which consider a D_{a} ray, toroidal plasma current I_{P} of$\sim$ 500 kA, lower hybrid current drive (LHCD) power of

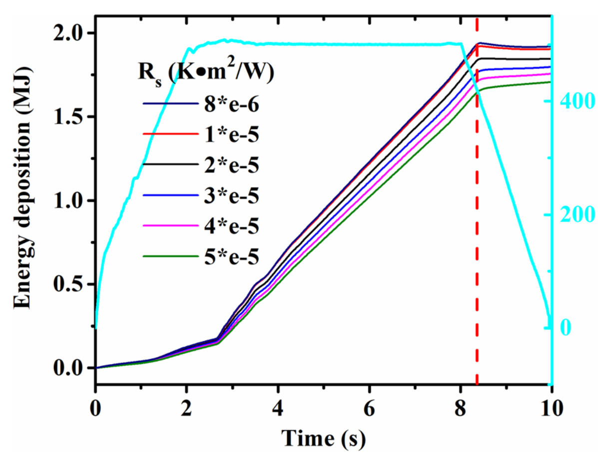

Fig. 8 Time evolution of energy deposition for different R_{s} numbers corresponding to shot #56028

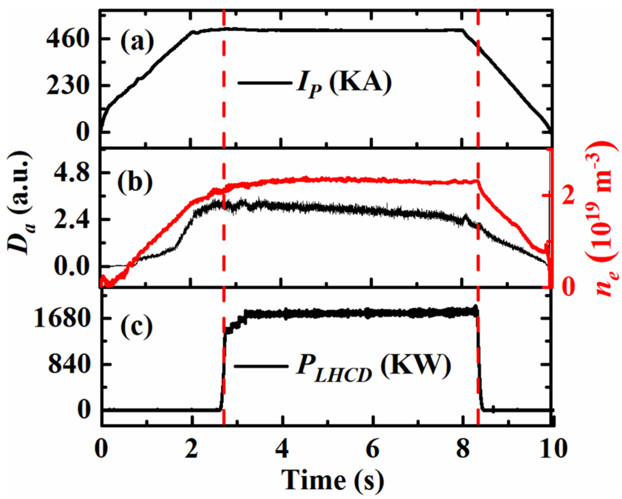

Fig. 9 Discharge parameters and the time evolution of heat flux in the LDTP for shot #56028. **a** Plasma current I_p. **b** The D_a ray (black line) and the n_e density (red line). **c** The LHCD power

1.7 MW at 2.7 s $\sim$ 8.4 s, central line-averaged density n_e of $\sim 2.5 \times 10^{19}$ m^{-3}. Under these discharge conditions, the heat fluxes calculated through the proposed method and the DFLUX code are shown in Fig. 10a and b, respectively. The general trends of heat flux determined by the two methods are similar, and the heat fluxes observed during the LHCD operation are generally high. Two areas (target location at 0.08–0.14 m and a target location at 0.21–0.22 m), which correspond to the second peak heat flux (SPHF) area and the original strike point (OSP) area described in other studies [14–16], reveal high heat fluxes. These results prove the validity of the method proposed in this study.

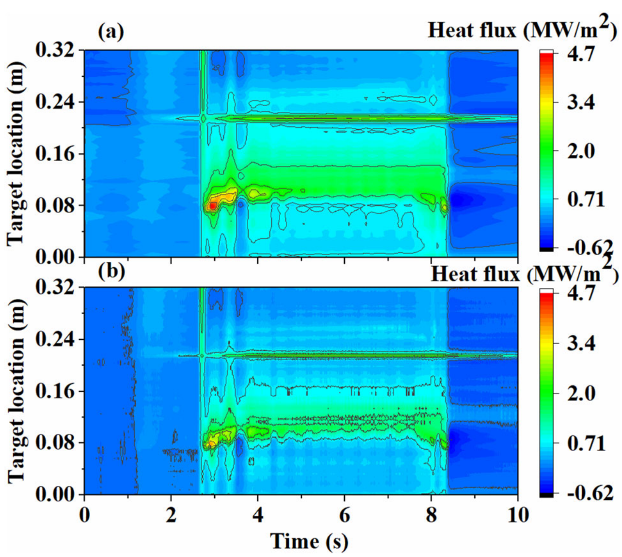

Fig. 10 (Color online) Heat flux result. **a** The proposed method. **b** DFLUX code

To further compare the results obtained by these two methods, the heat flux result at 0.10 m is shown in Fig. 11. From the figure, we can find that the change trend of heat flux results in these two methods is the same; however, the result obtained by the method in this study is a little higher than that in DFLUX. At present, the DFLUX program is the only heat flux calculation program available for EAST; thus, there are no more authoritative heat flux data to prove which method is better. Moreover, the average heat flux (AHF), AHF during LHCD, and maximum heat flux (MHF) of the two methods are compared in Fig. 12.

5 Conclusion

We introduced a finite element method to obtain the heat flux in the LDTP of EAST. Here, an IR diagnostic system is used to obtain the surface temperature. As the temperature obtained by the IR camera cannot be used to calculate the heat flux directly because of material emissivity, the IR transmissivity of the endoscope system, and the response function of the IR camera, the detected temperatures were calibrated to the temperatures read by the built-in thermocouple of EAST. A heat flux calculation model was created according to the physical structure of the LDTP, and a discretization of the modeling domain was generated. A heat conduction equation and boundary conditions were then obtained. A special thin layer that can affect the heat flux calculation was analyzed, and the thermal resistance of this layer was determined via a simple criterion in NSTX. Finally, this study compares the heat flux results of the proposed method with those determined by DFLUX. The general trends of heat flux are similar between the two methods. In summary, this study describes the complete

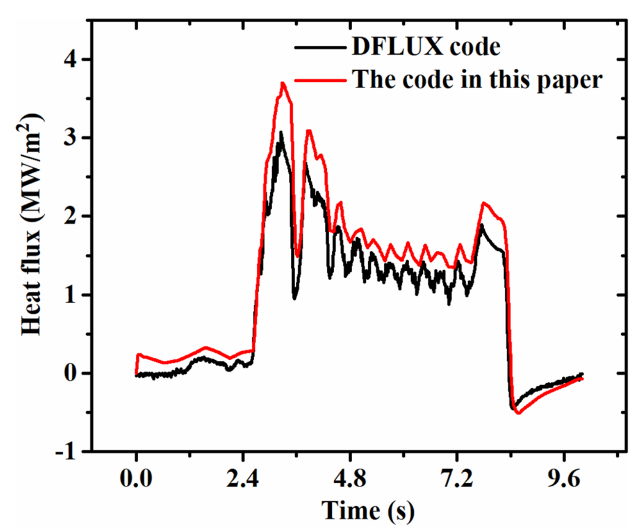

Fig. 11 Heat flux result at 0.10 m

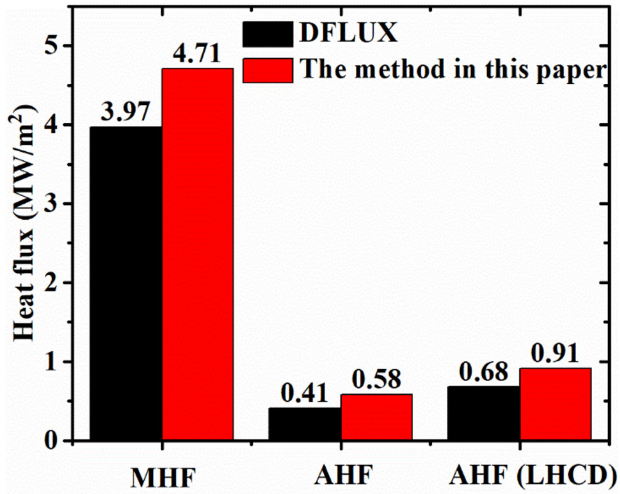

Fig. 12 Parameter comparison of the two methods

calculation process of a new method to determine the heat flux on the LDTP of EAST, which is significant for future analyses on this plate.

Acknowledgements The authors are grateful to all members of the EAST team for their contribution to the experiments.

References

1. Z.D. Yang, S.B. Shu, K.F. Gan et al., Calculation of the Heat Flux on the Frist Wall During Disruption on Tokamak. J. Fusion Energ. **36**, 15–20 (2017). https://doi.org/10.1007/s10894-016-0118-6
2. G. Arnoux, A. Loarte, V. Riccardo et al., Heat loads on plasma facing components during disruptions on JET. Nucl. Fusion **8**, 49 (2009). https://doi.org/10.1088/0029-5515/49/8/085038
3. K.F. Gan, M.H. Li, F.M. Wang et al., Hot spots generated by low hybrid wave absorption in the SOL on the EAST tokamak. J. Nucl. Mater. **438**, S364–S367 (2013). https://doi.org/10.1016/j.jnucmat.2013.01.069
4. C. Desgranges, M. Jouve, C. Balorin et al., Calibration procedures of the Tore-Supra infrared endoscopes. Nucl Instrum Methods Phys Res Sect A-Accel Spectrom Dect Assoc Equip **879**, 121–133 (2018). https://doi.org/10.1016/j.nima.2017.09.035
5. I. Balboa, G. Arnoux, T. Eich et al., Upgrade of the infrared camera diagnostics for the JET ITER-like wall divertor. Rev. Sci. Instrum. **83**, 10 (2012). https://doi.org/10.1063/1.4740523
6. B. Sieglin, M. Faitsch, A. Herrmann et al., Real time capable infrared thermography for ASDEX Upgrade System. Rev. Sci. Instrum. **11**, 86 (2015). https://doi.org/10.1063/1.4935580
7. J.W. Ahn, R. Maingi, D. Mastrovito et al., High speed infrared camera diagnostic for heat flux measurement in NSTX. Rev. Sci. Instrum. **81**, 4 (2010). https://doi.org/10.1063/1.3297899
8. Y. Gao, K.F. Gan, X.Z. Gong et al., Study of striated heat flux on EAST divertor plates induced by LHW using infrared camera. Plasma Sci. Technol **16**, 93–98 (2014). https://doi.org/10.1088/1009-0630/16/2/02
9. H. Yang, C.F. Wu, S. Dong et al., Performance comparison of the two ICRF antennas in EAST. Nucl. Sci. Tech. **27**, 46 (2016). https://doi.org/10.1007/s41365-016-0047-0
10. L. Tao, C.D. Hu, Y.L. Xie, Thermodynamic analysis and simulation for gas baffle entrance collimator of EAST-NBI system based on thermo-fluid coupled method. Nucl. Sci. Tech. **29**, 2 (2018). https://doi.org/10.1007/s41365-017-0349-x
11. F.K. Liu, B.J. Ding, J.G. Li et al., First results of LHCD experiments with 4.6 GHz system toward steady-state plasma in EAST. Nucl. Fusion **55**, 11 (2015). https://doi.org/10.1088/0029-5515/55/12/123022
12. Y. Zhang, Y.Z. Zhang, R.S. Lu et al., Investigation of the normal spectral band emissivity characteristic within 7.5 to 13 mu m for Molybdenum between 100 and 500 degrees C. Infrared Phys. Technol. **88**, 74–80 (2018). https://doi.org/10.1016/j.infrared.2017.11.017
13. L. del Campo, R.B. Perez-Saez, X. Esquisabel et al., New experimental device for infrared spectral directional emissivity measurements in a controlled environment. Rev. Sci. Instrum. **77**, 8 (2006). https://doi.org/10.1063/1.2393157
14. B. Zhang, K.F. Gan, X.Z. Gong et al., Study of divertor heat patterns induced by LHCD L-mode plasmas using an infra-red camera system on EAST. Plasma Sci. Technol **17**, 831–836 (2015). https://doi.org/10.1088/1009-0630/17/10/04
15. B. Shi, X.Z. Gong, W.H. Wang et al., Study on divertor heat flux of L-H transition with LHCD and NBI in EAST. Fusion Eng. Des. **123**, 778–782 (2017). https://doi.org/10.1016/j.fusengdes.2017.04.110
16. B. Shi, Z. Yang, B. Zhang et al., Heat flux on EAST divertor plate in H-mode with LHCD/LHCD + NBI. Chin. Phys. Lett. **34**, 095201 (2017). https://doi.org/10.1088/0256-307x/34/9/095201
17. K.F. Gan, J.W. Ahn, J.W. Park et al., 2D divertor heat flux distribution using a 3D heat conduction solver in National Spherical Torus Experiment. Rev. Sci. Instrum. **84**, 8 (2013). https://doi.org/10.1063/1.4792595
18. A. Herrmann, W. Junker, K. Gunther et al., Energy flux to the ASDEX-Upgrade diverter plates determined by thermography and calorimetry. Plasma Phys. Controlled Fusion **37**, 17 (1995). https://doi.org/10.1088/0741-3335/37/1/002